

Noise of Counter-rotation Propellers

Donald B. Hanson*

Hamilton Standard, United Technologies Corporation, Windsor Locks, Connecticut

Theory is presented for noise generation of counter-rotation (CR) propellers with special emphasis given to the effects of acoustic and aerodynamic interference between the two rotors. New radiation formulas are given for noise caused by unsteady loading. Spinning mode characteristics similar to those of turbofans are explicitly displayed so that reinforcements and cancellations between acoustic fields of two rotors or between acoustic modes of one rotor can be studied. Mode orders and cutoff criteria are compared with well-known results from spinning mode theory of turbofans. A theoretical wake model is also presented so that the roles of viscous and potential flow can be seen. The potential wake, which is ordinarily negligible in turbofans, is more powerful for CR propellers because of the smaller blade numbers and the strong load gradient at the blade tips. Noise predictions for an existing CR propeller airplane are compared with experimental results.

Nomenclature

a	$= \pi/J$
B, B_1, B_2	$=$ numbers of blades on rotors
B_D	$=$ chord-to-diameter ratio
BPF	$=$ blade passing frequency
c_0	$=$ ambient speed of sound
C_L	$=$ lift coefficient
C_{Dk}, C_{Lk}	$=$ k th drag (lift) harmonic coefficient
D	$=$ propeller diameter
FA	$=$ face alignment (Fig. 3)
$H_n^{(1)}$	$=$ Hankel function
I_n, K_n	$=$ modified Bessel functions
J	$=$ advance ratio
J_n	$=$ Bessel function
k	$=$ order of load harmonic
k_x, k_y	$=$ wavenumbers defined after Eqs. (1), (6), (11)
m	$=$ sound harmonic
M_r	$=$ blade section relative Mach number
M_T	$=$ blade tip rotational Mach number
M_x	$=$ flight Mach number
MCA	$=$ midchord alignment (Fig. 3)
N_1, N_2	$=$ rotational frequencies of rotors, $N_1 = \Omega_1/2\pi$
r, r_l	$=$ distances (Fig. 4)
t	$=$ time
z_0, z	$=$ source, observer radius/tip radius
$z_<, z_>$	$=$ lesser, greater of z_0, z
δ, δ'	$=$ Dirac delta function and its derivative
ϕ, θ	$=$ observer angles (Fig. 4)
$\phi^{(2)}$	$=$ blade location at $t=0$
ϕ_0, ϕ_s	$=$ phase angles associated with offset and sweep
ρ_0	$=$ ambient density
$\Omega, \Omega_1, \Omega_2$	$=$ rotor angular speeds
Ω_{12}	$= \Omega_1/\Omega_2$
ψ_k	$=$ Fourier transform of generalized source function
Ψ_{Dk}, Ψ_{Lk}	$=$ transforms of chordwise distributions of drag and lift (nondimensional)

Introduction

PROP-FANS (advanced turboprops) have been under development for some time as fuel conservative propulsors for transport aircraft. Representative single-rotation designs are projected to use about 20% less fuel than future generation turbofans for equivalent missions. Furthermore, an optimized counter-rotation (CR) prop-fan shown in Fig. 1 may save an additional 8% in fuel burned by eliminating the swirl left in the propeller wake. Since there are major projects in progress to develop a CR prop-fan suitable for powering commercial transport airplanes, a basic noise theory is needed for the design of CR prop-fans and analysis of test results.

The foundations of counter-rotation propeller noise analysis were laid in 1948 by Hubbard.¹ He recognized the major interference mechanisms and conducted tests to demonstrate the associated noise. This paper reproduces and extends some of Hubbard's analytical results and explores some of the aerodynamic interference issues using current turboprop terminology. Theory to deal with those issues was presented recently by the author² and forms the basis for the present paper. Reference 2 develops a helicoidal surface theory for propellers that treats unsteady, compressible aerodynamics and acoustics in a unified analysis. Blade forces are modeled in the classic manner as steady or unsteady doublet distributions convected in helicoidal paths determined by the advance and rotation of the propeller.

A distinction must be made between acoustic interference and aerodynamic interference. Noise radiated by each rotor of the prop-fan can be computed separately; when the two noise fields are added, the signals add constructively at some field points and destructively at others. The resulting effect is called acoustic interference. Aerodynamic interference, on the other hand, relates to the unsteady loading produced on one rotor due to operating in the nonuniform flowfield of the other.

Unsteady Loading Noise

This section presents far-field formulas for noise of one rotor due to its unsteady loading. The general case given first deals with loading that could be caused by interaction with any harmonic distortion including that caused by another rotor with a different rpm and a different number of blades. Then more specialized formulas are given for the CR propeller case with equal blade numbers and rpm on both rotors and also for the case of one rotor operating in a fixed distortion field as from a wing. In each case, the frequencies and modal patterns are discussed.

The loading sources for the radiation formulas are given in terms of the lift and drag harmonic coefficients C_{Lk} and C_{Dk}

Presented as Paper 84-2305 at the AIAA/NASA 9th Aeroacoustic Conference, Williamsburg, Virginia, Oct. 15-17, 1984; received Nov. 6, 1984; revision received March 15, 1985. Copyright © American Institute of Aeronautics and Astronautics, Inc., 1985. All rights reserved.

*Principal Research Engineer, Aircraft Systems Department. Member AIAA.

defined in the Appendix. For this section, it is necessary only to understand that C_{L0} and C_{D0} are the ordinary steady lift and drag coefficients at any radius and that the other coefficients relate to unsteady loading of harmonic order k . Also appearing in the noise equations are the factors Ψ_{Lk} and Ψ_{Dk} . These express chordwise interference effects and are such that the product $C_{Lk}\Psi_{Lk}$ is equivalent to a lift response function times the quasisteady lift coefficient. Parallel remarks apply to the product of C_{Dk} and Ψ_{Dk} .

Sweep and offset definitions are given in Fig. 2 along with the relevant Mach numbers. Observer coordinates in Fig. 3 are based on using the rear rotor as the reference rotor. Parameters without subscripts such as midchord alignment (MCA), face alignment (FA), chord/diameter B_D , and observer coordinates refer to the rear rotor, i.e., rotor 2. Ω_1 , Ω_2 , B_1 , and B_2 are the angular speeds and blade numbers for rotors 1 and 2. The following formulas for the acoustic pressure signal are derived in the Appendix.

Formulas for General CR Far-Field Case

$$p = \frac{-i\rho_0 c_0^2 B_2 \sin\theta}{8\pi(r_1/D)(1-M_x \cos\theta)} \sum_{m=-\infty}^{\infty} \sum_{k=-\infty}^{\infty} \exp \left\{ i \left[(mB_2 - kB_1) \left(\phi - \phi^{(2)} - \frac{\pi}{2} \right) + (mB_2 \Omega_2 + kB_1 \Omega_1) \left(\frac{r}{c_0} - t \right) \right] \right\} \\ \times \int_{\text{root}}^{\text{tip}} M_r^2 e^{i(\phi_0 + \phi_s)} J_{mB_2 - kB_1} \left[\frac{(mB_2 + kB_1 \Omega_{12}) z_0 M_T \sin\theta}{1 - M_x \cos\theta} \right] \left[k_x \frac{C_{Dk}}{2} \Psi_{Dk}(k_x) + k_y \frac{C_{Lk}}{2} \Psi_{Lk}(k_x) \right] dz_0 \quad (1)$$

where

$$k_x = \frac{2M_T}{M_r} \left[\frac{mB_2 + kB_1 \Omega_{12}}{1 - M_x \cos\theta} - kB_1 (1 + \Omega_{12}) \right] B_D \quad (2)$$

$$k_y = -\frac{2}{M_r} \left[\frac{(mB_2 + kB_1 \Omega_{12}) M_T^2 z_0 \cos\theta}{1 - M_x \cos\theta} - \frac{(mB_2 - kB_1) M_x}{z_0} \right] B_D \quad (3)$$

$$\phi_s = \frac{2M_T}{M_r} \left[\frac{mB_2 + kB_1 \Omega_{12}}{1 - M_x \cos\theta} - kB_1 (1 + \Omega_{12}) \right] \frac{\text{MCA}}{D} \quad (4)$$

$$\phi_0 = \frac{2}{M_r} \left[\frac{(mB_2 + kB_1 \Omega_{12}) z_0 M_T^2 \cos\theta}{1 - M_x \cos\theta} - (mB_2 - kB_1) \frac{M_x}{z_0} \right] \frac{\text{FA}}{D} \quad (5)$$

and Ω_{12} is the ratio of the two rotor speeds Ω_1/Ω_2 .

This waveform formula includes all noise and loading harmonics. The reader can verify for the steady load case ($C_{Dk} = C_{Lk} = 0$ for $k \neq 0$) that it reduces to previously published results.^{3,4} (Note that the sign convention for k_y has been changed from that in Refs. 3 and 4.)

For this general case with rpm and blade numbers not necessarily the same on the two rotors, it can be seen from the

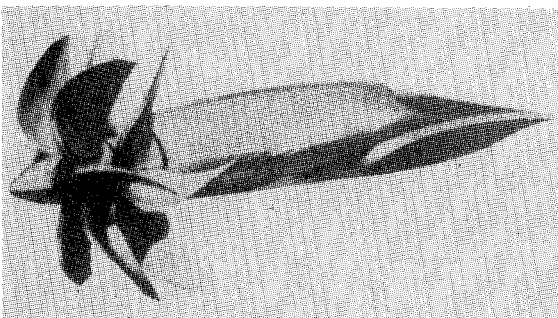


Fig. 1 Counter-rotation prop-fan.

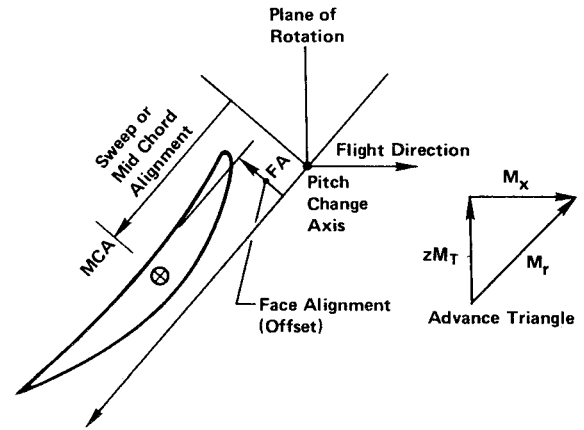


Fig. 2 Definition of sweep, offset, and Mach numbers.

form of the exponential that the observer will hear all frequencies $|mB_2 N_2 + kB_1 N_1|$, where m and k take on all integer values from $-\infty$ to $+\infty$. The circumferential mode order (number of lobes counted around the axis) can also be determined from the exponential in Eq. (1). It is given by the factor multiplying ϕ , in this case $(mB_2 - kB_1)$. If the upstream rotor were fixed ($\Omega_1 = 0$), Eq. (3) would resemble early compressor noise formulas with the mode order $(mB - kV)$ replaced here by $(mB_2 - kB_1)$ and with frequencies given by $|mB_2 N_2|$.

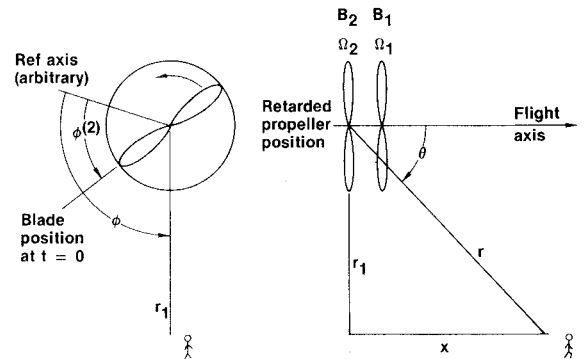


Fig. 3 Observer coordinates.

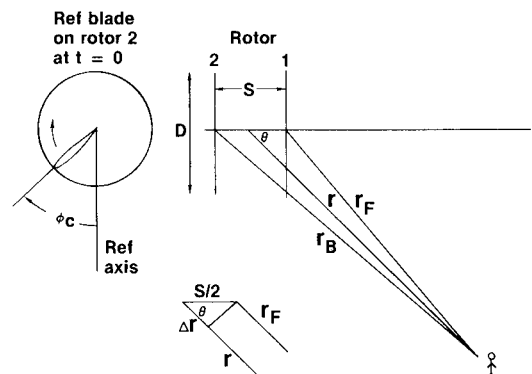


Fig. 4 Sketch for acoustic interference calculation.

Table 1 Mode orders and speed ratios for a 4×4 CR propeller

Sound harmonic, m	Load harmonic, k	Mode order, $(m-2k)B$	Speed ^a ratio, $m/(m-2k)$
1	-1	12	0.33
	0	4	1
	1	-4	-1
	2	-12	-0.33
2	-1	16	0.50
	0	8	1.00
	1	0	∞
	2	-8	-1.00
	3	-16	-0.50
3	-1	20	0.60
	0	12	1.00
	1	4	3.00
	2	-4	-3.00
	3	-12	-1.00
	4	-20	-0.60

^aSpinning mode speed/rotor speed, M_s/M_T .

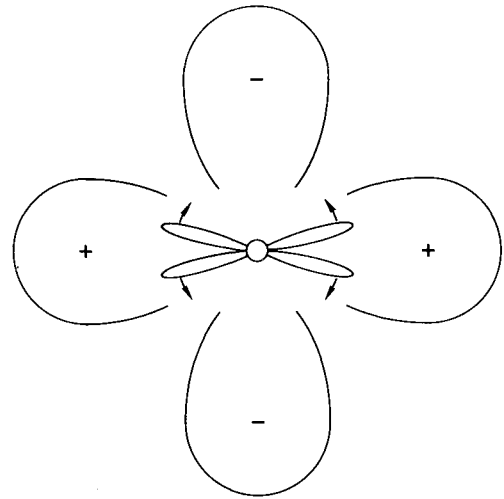


Fig. 5 Lobed standing wave pattern at blade passing frequency for a counter-rotation propeller with identical two-blade rotors fore and aft.

Formulas for CR Far-Field Case with $B_1 = B_2 = B$, $\Omega_1 = \Omega_2 = \Omega$

This special case for the same blade numbers and rpm on both rotors applies to most existing CR propellers. It was obtained from Eq. (1) by substituting $(m' = m + k)$, reordering the m summation, and then replacing m' with m .

$$p = \frac{-i\rho_0 c_0^2 B \sin\theta}{8\pi(r_1/D)(1-M_x \cos\theta)} \sum_{m=-\infty}^{\infty} \sum_{k=-\infty}^{\infty} \exp\left\{i\left[(m-2k)B\left(\phi - \phi^{(2)} - \frac{\pi}{2}\right) + mB\left(\frac{\Omega r}{c_0} - \Omega t\right)\right]\right\} \\ \times \int_{\text{root}}^{\text{tip}} M_r^2 e^{i(\phi_0 + \phi_s)} J_{(m-2k)B} \left(\frac{mBz_0 M_T \sin\theta}{1-M_x \cos\theta} \right) \left[k_x \frac{C_{Dk}}{2} \Psi_{Dk}(k_x) + k_y \frac{C_{Lk}}{2} \Psi_{Lk}(k_x) \right] dz_0 \quad (6)$$

where

$$k_x = \frac{2BM_T}{M_r} \left[\frac{m}{1-M_x \cos\theta} - 2k \right] B_D \quad (7)$$

$$k_y = -\frac{2B}{z_0 M_r} \left[\frac{m(M_r^2 \cos\theta - M_x)}{1-M_x \cos\theta} + 2kM_x \right] B_D \quad (8)$$

$$\phi_s = \frac{2BM_T}{M_r} \left[\frac{m}{1-M_x \cos\theta} - 2k \right] \frac{\text{MCA}}{D} \quad (9)$$

$$\phi_0 = \frac{2B}{z_0 M_r} \left[\frac{m(M_r^2 \cos\theta - M_x)}{1-M_x \cos\theta} + 2kM_x \right] \frac{\text{FA}}{D} \quad (10)$$

The sound frequencies are multiples of BPF of one of the rotors. Circumferential mode orders are given by $(m-2k)B$. For example, a four-blade rotor at BPF produces orders $4-8k = \dots -12, -4, 4, 12, \dots$ so that, despite the equal blade numbers, no zero-order modes are generated. Because the rear rotor cuts each wake from the front rotor twice per revolution, modes are generated with the same orders as a fan with $2B$ vanes. For $2 \times \text{BPF}$, however, the orders are $8-8k = \dots -16, -8, 0, 8, 16, \dots$, which includes a zero-order mode. (Zero-order modes are of concern because of their high radiation efficiency, as will be discussed below.)

Formulas for Far-Field Fixed-Distortion Case ($\Omega_{12} = 0$, $B_1 = 1$)

Of course, the fixed-distortion case has been treated by several authors in the past and analyses can be found in textbooks.^{7,8} It is presented here for completeness and comparison with the CR propeller results.

$$p = \frac{-i\rho_0 c_0^2 B \sin\theta}{8\pi(r_1/D)(1-M_x \cos\theta)} \sum_{m=-\infty}^{\infty} \sum_{k=-\infty}^{\infty} \exp\left\{i\left[(mB-k)B\left(\phi - \phi^{(2)} - \frac{\pi}{2}\right) + mB\left(\frac{r}{c_0} - \Omega t\right)\right]\right\} \\ \times \int_{\text{root}}^{\text{tip}} M_r^2 e^{i(\phi_0 + \phi_s)} J_{(mB-k)} \left(\frac{mBz_0 M_T \sin\theta}{1-M_x \cos\theta} \right) \left[k_x \frac{C_{Dk}}{2} \Psi_{Dk}(k_x) + k_y \frac{C_{Lk}}{2} \Psi_{Lk}(k_x) \right] dz_0 \quad (11)$$

where

$$k_x = \frac{2M_T}{M_r} \left[\frac{mB}{1 - M_x \cos \theta} - k \right] B_D \quad (12)$$

$$k_y = \frac{-2}{z_0 M_r} \left[\frac{mB(M_r^2 \cos \theta - M_x)}{1 - M_x \cos \theta} + kM_x \right] B_D \quad (13)$$

$$\phi_s = \frac{2M_T}{M_r} \left[\frac{mB}{1 - M_x \cos \theta} - k \right] \frac{MCA}{D} \quad (14)$$

$$\phi_y = \frac{2}{z_0 M_r} \left[\frac{mB(M_r^2 \cos \theta - M_x)}{1 - M_x \cos \theta} + kM_x \right] \frac{FA}{D} \quad (15)$$

Observed frequencies are again multiples of BPF. Mode orders are $(mB - k)$ as was found by other authors. Equation (11) would also apply to a prop-fan with V fixed vanes if k were replaced by kV .

Modal Efficiencies

For turbopfans and compressors, acoustic theory⁹ established a cutoff condition that determines whether a given spinning mode propagates or decays in a duct. For propellers there is a related condition better thought of as a reduction in radiation efficiency than as a sharp cutoff. In any of the noise equations presented earlier, the radiation efficiency for a mode with indices m, k is determined by properties of the Bessel function. In general, Bessel functions $J_n(x)$ decay rapidly for values of argument less than the order of the functions, i.e., for $|x| < |n|$. Thus, for the fixed-distortion case in Eq. (11), if we consider sound radiated at $\theta = 90$ deg from the blade tip ($z_0 = 1$), the low-efficiency criterion is $|mBM_T| < |mB - k|$ or

$$M_s = \left| \frac{mB}{mB - k} \right| M_T < 1 \quad \text{low efficiency criterion for fixed distortion} \quad (16)$$

In duct theory,⁹ M_s was identified as the rotational Mach number of the mode at the duct outer wall from the combination of parameters $(mB - k)\phi + mB\Omega t$ appearing in the exponential of Eq. (11). Cutoff required this to be less than some number in the range 1-1.8, depending on mode order. For propellers, we can call M_s the spinning mode tip Mach number.

For an example of the use of Eq. (16), consider an eight-bladed prop-fan operating in yaw so that the dominant unsteady loading component will be at $k = 1$. At BPF ($m = 1$), Eq. (16) gives $M_s = (8/7)M_T$. Since this is not substantially higher than the steady load ($k = 0$) condition, $M_s = M_T$, the rotor noise levels should not be too sensitive to yaw. For increasing distortion orders ($k > 1$), Eq. (16) will no longer be satisfied and efficient radiation can occur. Of course, the noise level will depend on the strength of the load harmonics C_{Lk} and C_{Dk} .

For the special CR propeller case in Eq. (6) where the blade numbers and rpm on both rotors are the same, the low-efficiency condition is different, namely, $|mBM_T| < |m - 2k|B$ or

$$M_s = \left| \frac{m}{m - 2k} \right| M_T < 1 \quad \text{low efficiency criterion for CR propeller} \quad (17)$$

Table 1 treats this function for the case of a 4×4 CR propeller. The last column gives the speed ratio $M_s/M_T = m/(m - 2k)$ for the various sound and load harmonics. The reader must supply the rotor tip Mach number M_T for his hardware in order to apply Eq. (17). For BPF ($m = 1$), Table 1 shows that the highest efficiency modes are for steady loading ($k = 0$)

and the first unsteady harmonic ($k = 1$). These modes spin in opposite directions, but have the same efficiency. However, in most applications, the steady load coefficients should be much larger than those for $k = 1$ so that unsteady loading is not a significant noise source at BPF. At $2 \times$ BPF, however, the $k = 1$ load harmonic produces a zero-order mode that is much more efficient than the steady loading mode for subsonic tip speeds. For high enough tip speed and high steady loading, the steady loading mode will dominate. However, for low tip speed and loading, the zero lobe $k = 1$ mode must take over. For higher harmonics of BPF, Table 1 shows that more and more mode orders become efficient so that, in general, unsteady loading is a more important source at high frequency.

Acoustic Interference

The noise field of a CR propeller is computed as the sum of the fields from each rotor with the assumption that linear superposition applies. If the noise from each rotor has the same frequency, then standing wave patterns around the axis of rotation can be produced through the constructive and destructive process of acoustic interference. This is the well-known case analyzed by Hubbard.¹ However, it does not seem to have been recognized that two spinning modes from the same rotor can also produce a circumferential standing wave pattern. These two acoustic interference cases (inter-rotor and intermode) can produce circumferential directivity patterns whose differing characteristics may be useful for noise source diagnosis, as discussed below.

Inter-rotor Acoustic Interference

Aerodynamic interference and the associated unsteady loading should be included in calculation of noise of each rotor; however, at the lower harmonics these effects may be small and it is worthwhile to illustrate the inter-rotor acoustic interference effect with the steady loading formulas only.

In Eq. (11), the first exponential describes the radial and circumferential propagation of waves. For steady loading at the m th sound harmonic, this reduces to

$$F_2 = \exp i \left[mB(\phi - \phi^{(2)}) + \Omega \left(\frac{r}{c_0} - t \right) \right] \quad (18)$$

To interpret Eq. (18), note that for constant r the factor $(\phi - \Omega t)$ indicates waves spinning at angular speed Ω , i.e., locked to the rotor. At constant ϕ , the factor $(r - c_0 t)$ indicates propagation away from the retarded position at the ambient sound speed c_0 .

In Fig. 4, the radiation distances r for the front and back rotors are assigned the values r_F and r_B . The angle at which the two rotors cross (at $t = 0$) is ϕ_c from the reference axis measured in the direction of rotation of the rear rotor, i.e., $\phi^{(2)} = \phi_c$. For the front rotor, the $t = 0$ angle is $\phi^{(1)} = -\phi_c$ because the angle on each rotor is measured in the direction of its rotation. Thus, for the rear rotor Eq. (18) becomes

$$F_2 = \exp i \left[mB(\phi - \phi_c) + \Omega \left(\frac{r_B}{c_0} - t \right) \right] \quad (19)$$

For the front rotor, we switch the sign on ϕ to the rear rotor system with the result

$$F_1 = \exp i \left[mB(-\phi + \phi_c) + \Omega \left(\frac{r_F}{c_0} - t \right) \right] \quad (20)$$

At the bottom in Fig. 4 is shown the far-field condition $r_F = r - \Delta r$, where $\Delta r = (S/2)\cos\theta$. Similarly, $r_B = r + \Delta r$. Com-

binning these equations and the definition $M_T = \Omega r_T / c_0$ leads to

$$F = F_1 + F_2 = 2 \cos \left[mB \left(\phi - \phi_c + \frac{S}{D} M_T \cos \theta \right) \right] \exp \left[imB \Omega \left(\frac{r}{c_0} - t \right) \right] \quad (21)$$

showing traveling waves in the r direction and a standing pattern in the ϕ direction. Near the plane of rotation $(S/D)M_T \cos \theta$ can be neglected leaving $2 \cos [mB(\phi - \phi_c)]$, which was the interference effect found by Hubbard¹ via a different argument. The function indicates twice the amplitude of a single rotor at the blade crossing azimuths and complete cancellation between, as sketched in Fig. 5. Note that, because the cosine function has two peaks and two nodes per cycle, the circumferential standing wave pattern has $2mB$ lumps around the axis.

To show that the axial separation effect, via $(S/D)M_T \cos \theta$, in Eq. (21) is not always negligible, calculations were made for the geometry used in a recent wind tunnel test at NASA Langley.¹⁰ The two four-blade rotors were geared for synchronous rpm with the blade crossing points as shown at the top in Fig. 6. The lower part of the figure shows the interference correction pattern computed from Eq. (21) with a correction for differing propagation distances to different microphones. The shape of the interference curve agrees quite satisfactorily with the data, including the small shift to the right due to axial separation. If the axial spacing term were neglected, the theoretical curve would be symmetrical about the center microphone position.

The same inter-rotor acoustic interference was exhibited in recent tests by Hamilton Standard of the Fairey Gannet CR propeller airplane shown in Fig. 7. The microphone boom was at a fixed circumferential location, but a small difference in rotor rpm was used to sweep the circumferential directivity pattern past the microphone. Figure 8 shows the patterns for the first four harmonics. As predicted by Eq. (21), the number of lumps per circumference is proportional to the order of the sound harmonic for the first few harmonics.

Intermode Acoustic Interference

Here it is shown that two modes from the same rotor can interfere to produce circumferential standing wave patterns. Considering any two modes with indices k_1 and k_2 , define an average k and a Δk such that

$$k_1 = \bar{k} + \frac{1}{2} \Delta k, \quad k_2 = \bar{k} - \frac{1}{2} \Delta k \quad (22)$$

For simplicity, assume that the modes have equal amplitudes so that two phase factors from Eq. (6) can simply

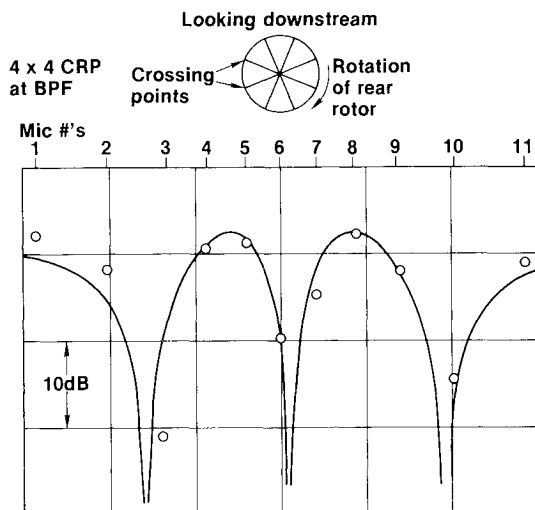


Fig. 6 Comparison of Block's circumferential directivity data with theory based on Eq. (23). Curves were shifted vertically for good fit.

be added, with the result

$$F = 2 \cos [B \Delta k (\phi - \phi^{(2)})] \times \exp \left\{ i \left[(m - 2\bar{k}) B (\phi - \phi^{(2)}) - mB \Omega \left(\frac{r}{c_0} - t \right) \right] \right\} \quad (23)$$

The standing wave behavior given by $2 \cos [B \Delta k (\phi - \phi^{(2)})]$ has a fundamental spatial frequency set by $\Delta k = 1$. This gives $2B$ lumps around the axis in the circumferential directivity at each sound harmonic in contrast with the $2mB$ lump result from inter-rotor interference.

Generation of a $2B$ circumferential pattern is reasonable from a physical viewpoint for a synchronous CR propeller when it is recognized that blades cross at $2B$ locations around the circumference. The crossing points are always the same and, since sound is radiated from these localized circumferential points, we should expect a circumferential directivity variation. A similar circumferential variation was predicted for fans with fixed vanes, as reported in Ref. 11.

The $2B$ circumferential directivity characteristic of intermode interference can be expected for CR propellers in circumstances where unsteady loading is important. For example, in Fig. 8, the fourth sound harmonic is beginning to show a $2B$ periodicity, indicating a switch from steady to unsteady loading dominance at this frequency and directivity point. Other CR propellers with lighter loading or lower speed may show the intermode behavior at lower harmonic order.

Aerodynamic Interference

If the effect of the rear rotor on the front rotor is ignored, then evaluation of aerodynamic interference requires computation of the nonuniform wake from the front rotor and the associated unsteady lift response of the rear rotor.

Lift response theories have received a great deal of attention in studies of compressors and will not be discussed in any detail here except to mention that Hamilton Standard currently uses an isolated airfoil gust response function of Amiet.¹² Wakes will be discussed further, however, because they have received less attention for unshrouded rotors.

To aid in analysis of data and in analytical modeling, it is useful to categorize the various wake generation phenomena. The first division is into viscous and potential effects. Viscous wakes develop as the retarded flow in the blade boundary layers is shed off the trailing edges. Potential flow, with the exception of strong shocks, covers the rest of the field and is, in principle, calculable from potential theory. Potential effects can be further subdivided into bound, radiating, and trailing categories. The bound field includes thickness, circulation,

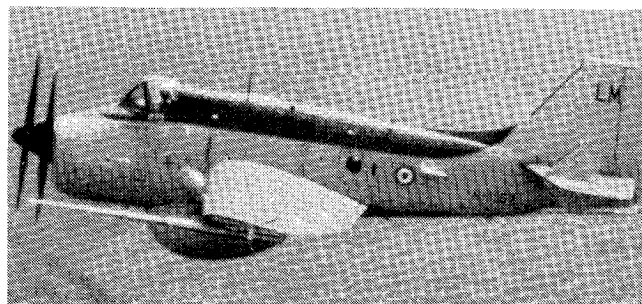


Fig. 7 Fairey Gannet modified for acoustic tests.

and shocks whose influence can extend upstream as well as downstream. Bound effects decay rapidly with distance from the rotor and may not be too important in aerodynamic interaction of CR propellers if supercritical section speeds can be avoided by the use of thin blades and sweep. Similarly, radiation is primarily outward and may not produce significant unsteady loading on adjacent rotors. The trailing wake is caused by lift on the blades and would persist undiminished behind the rotor in the absence of viscous absorption.

Some of these effects can be seen in Fig. 9, which shows a hot-wire anemometer measurement of the tangential velocity component 5 cm behind a two-blade SR-3 model propeller in the acoustic wind tunnel at the United Technologies Research Center. A very short-wire and a high-frequency response data acquisition system were used to be sure of resolving the narrow viscous wake. In fact, the figure clearly shows the viscous wake superimposed on the potential part.

In turbofan methods it is legitimate to neglect the trailing potential wake because it is indeed small compared to the viscous velocity defects. However, for propellers, the smaller number of blades and the strong radial loading gradient near the tips cause much larger potential variations. The trailing potential wake is treated in more detail in the following paragraphs.

In Ref. 5, Eqs. (26) and (27) gave the downward angle in the far potential wake as measured at the vortex sheets ($\phi=0$). When the ϕ variation is restored by including the factor $\cos mB\phi$, the formula becomes

$$\alpha = \int_{\text{root}}^{\text{tip}} B_D C_L \frac{B^3 \sigma_0^3}{\pi Z Z_0} \sum_{m=1}^{\infty} m^2$$
$$\times I_{mB}(mB\alpha_{<}) K_{mB}(mB\alpha_{>}) \cos mB\phi \, dz_0 \quad (24)$$

As was explained in Ref. 5, this treats any radial load distribution and gives the same wake as the classic Goldstein propeller aerodynamic theory¹³ for the special case of an optimum distribution of $B_D C_L$.

A plot of the wake from Eq. (24) is given in Fig. 10 for the four-blade case listed in Goldstein's original paper. The

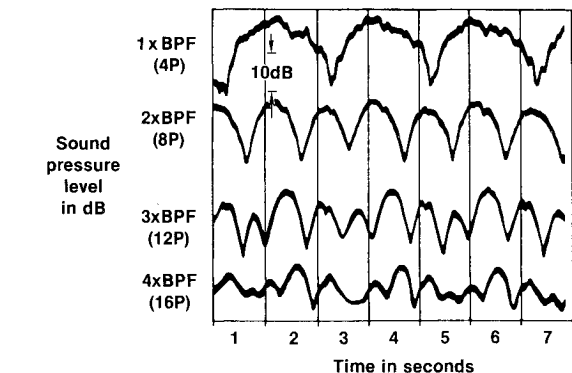


Fig. 8 Gannet CR propeller circumferential directivity.

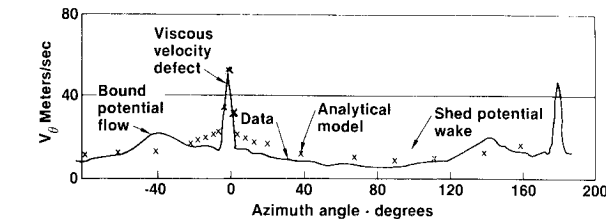


Fig. 9 Tangential velocity component behind two-blade SR-3 propfan model at 0.7 radius ratio, $M_x=0.32$, rpm = 11,350.

abscissa represents azimuth angle ϕ or blade-to-blade angular distance. Only one-half a blade gap is shown; the curves are symmetric about $\phi=0$. It can be seen in Fig. 10 at the midspan stations that the blade-to-blade variation is very small, but that the mean swirl is large. However, near the tip, the mean swirl drops rapidly and the blade-to-blade variation becomes very strong. In fact, for radius ratios passing through 1, the downwash pulse flips over showing the properties of a tip vortex. It should be noted that this model includes a vortex sheet at the cusp in the figure. However, the sheet does not roll up into a tip vortex; rather, it lies undistorted on the propeller advance surface. Thus, the vorticity is entirely accounted for, but its geometry is approximate. This approximation may be

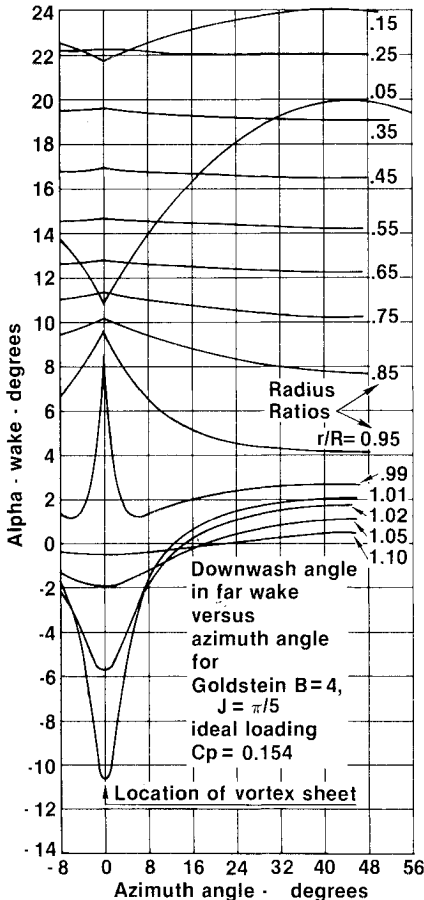


Fig. 10 Far potential wake of a four-blade propeller.

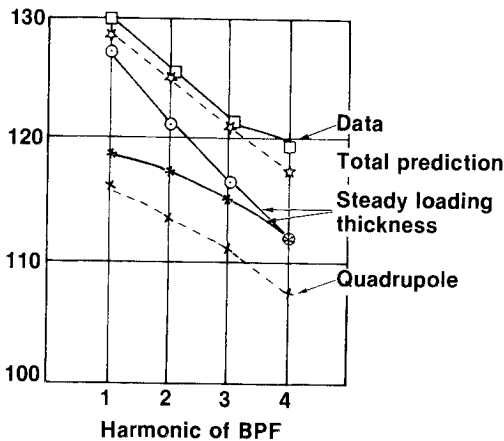


Fig. 11 Theory/test comparison for Gannet flight test at 100% power (microphone in plane of rear rotor).

acceptable at reasonable forward flight conditions, but is undoubtedly poor at low flight speed.

A wake model was generated at Hamilton Standard for use in a contract study on counter-rotation propellers¹⁴ comprising the trailing potential flow from Eq. (24) and the Silverstein viscous wakes.¹⁵ The lift input for the potential flow and the drag for the viscous wake were generated by one of the propeller aerodynamic design codes at Hamilton Standard. Comparison with data as shown in Fig. 9 shows excellent agreement in the viscous portion. The shed potential wake agrees well in shape, but is overpredicted in magnitude, apparently because the lift coefficient input to Eq. (24) was too large. The extra bump in the wake data that is not predicted by the model appears to be a bound potential effect due to blade thickness and is not yet included in the wake prediction model.

Noise Calculations

Calculations using the above theory have been made for comparison with data from Hamilton Standard's Fairey Gannet aircraft with a "conventional" CR propeller. The aircraft shown in Fig. 7 was equipped with a microphone boom and operated to obtain noise data under normal flight conditions. In Fig. 11, data from a microphone in the plane of rotation of the rear rotor are compared with predictions (including thickness and quadrupole components) using formulas from Ref. 3. Noise caused by unsteady loading was computed, but its contribution was so low as to be off scale in Fig. 11. The excellent agreement in this figure generally indicates that noise near the plane of rotation due to aerodynamic interaction was low at these frequencies. Noise at the higher harmonic orders and at forward directivity points was underpredicted, suggesting that the aerodynamic interference model needs to be refined.

Conclusions

A theoretical framework has been provided for analysis and prediction of noise from counter-rotation propellers. It includes analytical models for the aerodynamic unsteady interaction between rotors and for the noise from the resulting unsteady blade loads.

Aerodynamic interaction sources are categorized as viscous wakes, trailing potential wakes, and bound potential effects. None of these is negligible with CR propellers. Agreement of predictions from the analytical wake model with hot wire measurements is good.

Acoustic interference was divided into inter-rotor interference, involving the acoustic fields of both rotors, and intermode interference, involving modes from one rotor. The resulting circumferential directivity is different for the two phenomena and can be valuable in noise source diagnosis. Circumferential directivity from a recent noise test was well predicted by the interference model.

Calculations and comparisons with noise data so far indicate that aerodynamic interference is not the dominant source of noise near the plane of rotation for the first few harmonics of blade passing frequency. For an existing conventional CR propeller, aerodynamic interference does appear to be a significant noise source at higher harmonics and forward of the plane of rotation.

Appendix: Derivation of Far-Field Radiation Formula

This Appendix gives the derivation of Eq. (1) based on theory previously presented in Ref. 2. The starting point is the near-field equation for radiation from any helically convected time-harmonic source distribution. Required steps in the derivation include passing to the far field, introducing the unsteady lift and drag forces, identifying the correct blade loading frequencies, and accounting for multiple blades on the rotor. The resulting equation gives the noise radiated by a single rotor due to unsteady load harmonics that are assumed known from a separate analysis. For a counter-rotation propeller, noise from the two rotors must be added.

Far-Field Limit

In Ref. 2, Eq. (25) gave the pressure signal for a one-bladed rotor with source frequency $\omega_k/2\pi$ and angular speed Ω_2 as

$$p_k(r, \phi, x_l, t) = \frac{i}{8\pi V} \iint \sum_{n=-\infty}^{\infty} \exp\{i[n(\phi - \Omega_2 t) - \omega_k t]\} \exp\left[i\frac{\omega - n\Omega_2}{V} x_l\right] \\ \times J_n(\mu r_0) H_n^{(1)}(\mu r) \psi_k\left(\frac{\bar{\omega}}{U_0}, \xi_0, r_0\right) \exp\left[-i(\bar{\omega} - n\Omega_2) \frac{\Omega_2 r_0 \xi_0}{V U_0}\right] \exp\left[\frac{inV\xi_0}{r_0 U_0}\right] d\xi_0 d\bar{\omega} dr_0 \quad (A1)$$

where

$$\mu = \sqrt{\left(\frac{\bar{\omega} + \omega_k}{c_0}\right)^2 - \left(\frac{\bar{\omega} - n\Omega_2}{V}\right)^2} \quad (A2)$$

The observer cylindrical coordinates are r, ϕ, x_l and the source helicoidal coordinates are r_0, ξ_0, γ_0 . γ_0 (which appears later) is measured backward from the blade pitch change axis along the advance helix at constant radius. ξ_0 is the coordinate normal to γ_0 at a constant radius. The flight speed is V and a blade section advance speed is given by $U_0 = \sqrt{V^2 + \Omega_2^2 r_0^2}$. ψ_k is a wavenumber description of the source to be defined below.

The far-field equivalent of Eq. (A1) can be derived by first shifting and normalizing the wavenumber variable according to $\bar{\omega} = (\omega\Omega_2 - \omega_k)$ and then performing the ω integral by the method of stationary phase. The procedure is exactly the same as given in the Appendix of Ref. 6 with the stationary phase point for ω given by $(n + \omega_k/\Omega_2)/(1 - M_x \cos\theta)$. The analysis need not be repeated here, but the result for $r \gg r_T$ is

$$p_k = \frac{\sin\theta}{8\pi(r_l/D)(1 - M_x \cos\theta)} \iint \sum_{n=-\infty}^{\infty} \exp\left\{i\left[n\left(\phi - \frac{\pi}{2}\right) + (n\Omega_2 + \omega_k)\left(\frac{r}{c_0} - t\right)\right]\right\} \psi_k\left[\frac{1}{U_0}\left(\frac{n\Omega_2 + \omega_k M_x \cos\theta}{1 - M_x \cos\theta}\right), \xi_0, r_0\right] \\ \times J_n\left[\frac{(n + \omega_k/\Omega_2)z_0 M_T \sin\theta}{1 - M_x \cos\theta}\right] \exp\left\{i\left[\frac{nM_x}{z_0 M_r} - (n + \omega_k/\Omega_2) \frac{z_0 M_r^2 \cos\theta}{M_r(1 - M_x \cos\theta)}\right] \frac{\xi_0}{r_T}\right\} d\xi_0 dz_0 \quad (A3)$$

where the velocities have now been normalized by the ambient sound speed c_0 according to $V = c_0 M_x$, $U_0 = c_0 M_r$, and $\Omega_2 r_T = c_0 M_T$. For convenience, the source position is given in terms of retarded (or radiation) angle θ and r_l is the sideline distance as sketched in Fig. 3.

Loading Frequencies

For an upstream rotor with B_l blades and angular speed Ω_l , frequency on a downstream blade is given by

$$\omega_k = k B_l (\Omega_l + \Omega_2) \quad (A4)$$

for the k th harmonic of unsteady loading. For fixed distortion, $\omega_k = k \Omega_2$. In both cases, we must sum on all integer values of k from $-\infty$ to $+\infty$. In the following, we treat only the counter-rotation case; the fixed distortion case can be obtained from it by setting $\Omega_l = 0$ and $B_l = 1$.

Unsteady Source Representation

In Refs. 2-6 source distributions are represented in the frequency domain by their Fourier transforms,

$$\psi_k \left(\frac{\omega}{U_0}, \xi_0, r_0 \right) = \int_{-\infty}^{\infty} g(\gamma_0, \xi_0, r_0) \exp \left(i \frac{\omega}{U_0} \gamma_0 \right) d\gamma_0 \quad (A5)$$

where g is a generalized source distribution including thickness, loading, and quadrupole terms. For the task at hand, the lift and drag sources are selected from the generalized source function given by Eq. (13) of Ref. 2 to yield

$$g_k(\gamma_0, \xi_0, r_0) = \frac{\partial}{\partial \gamma_0} [D(\gamma_0, r_0)]_k \delta(\xi_0 + \text{FA}) + [\Delta P(\gamma_0, r_0)]_k \delta'(\xi_0 + \text{FA}) \quad (A6)$$

where $[D(\gamma_0, r_0)]_k \exp(-i\omega_k t)$ and $[\Delta P(\gamma_0, r_0)]_k \exp(-i\omega_k t)$ are the drag and lift forces per unit area at load harmonics k . FA is the section face alignment, or offset, defined in Fig. 3. The Fourier series giving the load waveform in terms of harmonics is

$$\Delta P(\gamma_0, r_0, t) = \sum_{k=-\infty}^{\infty} [\Delta P(\gamma_0, r_0)]_k e^{-i\omega_k t} \quad (A7)$$

where $[\Delta P(\gamma_0, r_0)]_0$ is the steady loading component $\Delta P(\gamma_0, r_0)$ of Ref. 3.

Substitution of g_k into Eq. (A5) gives the frequency domain source representation

$$\psi_k \left(\frac{\omega}{U_0} \right) = \delta(\xi_0 + \text{FA}) \int_{-\infty}^{\infty} \frac{\partial}{\partial \gamma_0} [D(\gamma_0, r_0)]_k e^{i\omega \gamma_0 / U_0} d\gamma_0 + \delta'(\xi_0 + \text{FA}) \int_{-\infty}^{\infty} [\Delta P(\gamma_0, r_0)]_k e^{i\omega \gamma_0 / U_0} d\gamma_0 \quad (A8)$$

Integration by parts in the first term gives

$$\psi_k \left(\frac{\omega}{U_0} \right) = -\delta(\xi_0 + \text{FA}) i \frac{\omega}{U_0} \int_{-\infty}^{\infty} [D(\gamma_0, r_0)]_k e^{i\omega \gamma_0 / U_0} d\gamma_0 + \delta'(\xi_0 + \text{FA}) \int_{-\infty}^{\infty} [\Delta P(\gamma_0, r_0)]_k e^{i\omega \gamma_0 / U_0} d\gamma_0 \quad (A9)$$

In parallel with Eqs. (39) and (40) of Ref. 3, we define the functions f_D and f_L according to

$$[D(\gamma_0, r_0)]_k = \frac{\rho_0 U_0^2}{2} C_{Dk} f_{Dk} \left(X - \frac{\text{MCA}}{b} \right) \quad (A10)$$

$$[\Delta P(\gamma_0, r_0)]_k = \frac{\rho_0 U_0^2}{2} C_{Lk} f_{Lk} \left(X - \frac{\text{MCA}}{b} \right) \quad (A11)$$

where X is the nondimensional chordwise distance that runs from -0.5 at the leading edge and to $+0.5$ at the trailing edge and the f are factors with unit areas that give the shape of the load distributions. MCA is a midchord alignment, or sweep, as defined in Fig. 3. C_{Dk} and C_{Lk} are the drag and lift harmonics.

Note that the form of Eq. (A11) implies that the lift distribution is in phase from the leading edge to the trailing edge at any radial station. This choice was made at Hamilton Standard because our initial applications of this theory used compressible lift response functions whose chordwise pressure distributions are not given explicitly in the literature. Thus, the lift response functions are used to compute the amplitude and phase of C_{Lk} , but f_{Lk} is approximated by a two-dimensional steady calculation. However, the ultimate application of this noise theory is in conjunction with the unsteady lifting surface theory of Ref. 2. Because solution of the lifting surface integral equation requires dividing the chord into many panels (each with constant phase), the form of Eq. (A11) is well suited to panel methods.

When Eqs. (A10) and (A11) are substituted into Eq. (A9) and a shift in integration variable is made, the desired frequency domain loading representation becomes

$$\begin{aligned} \psi_k \left(\frac{\omega}{U_0} \right) &= \frac{\rho_0 U_0^2}{2} b \exp \left[i \frac{2\omega r_T}{U_0} \frac{\text{MCA}}{D} \right] \\ &\times [-\delta(\xi_0 + \text{FA}) \frac{i\omega}{U_0} C_{Dk} \Psi_{Dk}(k_x) \\ &+ \delta'(\xi_0 + \text{FA}) C_{Lk} \Psi_{Lk}(k_x)] \end{aligned} \quad (A12)$$

where $k_x = \omega b / U_0$, b = airfoil chord, and

$$\Psi_{Dk}(k_x) = \int_{-1/2}^{1/2} f_{Dk}(X) e^{ik_x X} dX \quad (A13)$$

$$\Psi_{Lk}(k_x) = \int_{-1/2}^{1/2} f_{Lk}(X) e^{ik_x X} dX \quad (A14)$$

are the nondimensional noncompactness factors analogous to Ψ_D and Ψ_L of Ref. 3. In fact, $\Psi_{D0} = \Psi_D$ and $\Psi_{L0} = \Psi_L$. Also, note for a chordwise compact source ($b = 0$) that Ψ_{Dk} and Ψ_{Lk} are unity since f_{Dk} and f_{Lk} have unit area by definition.

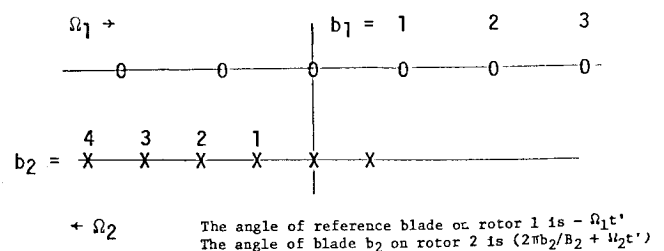


Fig. A1 Timing of blades b_1 and b_2 .

Equation (A12) can now be substituted back into Eq. (A3), permitting the ξ_0 integration to be performed. The result is

$$p_k = \frac{-i\rho_0 c_0^2 \sin\theta}{8\pi(r_1/D)(I - M_x \cos\theta)} \int M_r^2 \sum_{n=-\infty}^{\infty} \exp \left\{ i \left[n \left(\phi - \frac{\pi}{2} \right) + (n\Omega_2 + \omega_k) \left(\frac{r_0}{c_0} - t \right) + \phi_s + \phi_0 \right] \right\} \\ \times \left\{ \frac{M_T}{M_r} \left[\frac{n + (\omega_k/\Omega_2)}{I - M_x \cos\theta} - \frac{\omega_k}{\Omega_2} \right] B_D C_{Dk} \Psi_{Dk}(k_x) - \left[\left(n + \frac{\omega_k}{\Omega_2} \right) \frac{z_0 M_T^2 \cos\theta}{M_r (I - M_x \cos\theta)} - \frac{n M_x}{z_0 M_r} \right] B_D C_{Lk} \Psi_{Lk}(k_x) \right\} \\ \times J_n \left[\frac{(n + \omega_k/\Omega_2) z_0 M_T \sin\theta}{I - M_x \cos\theta} \right] dz_0 \quad (A15)$$

where

$$k_x = \frac{2M_T}{M_r} \left[\frac{n + (\omega_k/\Omega_2)}{I - M_x \cos\theta} - \frac{\omega_k}{\Omega_2} \right] B_D$$

ϕ_0 and ϕ_s , which are phase angles associated with offset and sweep, are defined later in Eqs. (A21) and (A22).

Effect of Multiple Blades

Equation (A15) gives the radiation from a one blade only. If we number the B_2 blades on rotor 2 in the direction of rotation with an index b_2 running from 0 to $(B_2 - 1)$, then Eq. (A15) applies to the $b_2 = 0$ blade. To obtain the signal for $b_2 \neq 0$, we must account for both point-of-action effects and timing effects. With regard to the point-of-action effect, the blades of an equispaced rotor are installed in the hub at azimuth angles $2\pi b_2/B_2$. Clearly, moving a blade from zero azimuth to $2\pi b_2/B_2$ is equivalent to reducing the observer azimuth by $2\pi b_2/B_2$. Thus, the point-of-action effect is accounted for by changing ϕ to $(\phi - 2\pi b_2/B_2)$ in Eq. (A15).

The timing of the source for blade 0 was given by $\exp(-i\omega_k t)$ in Eq. (A7). Blade b_2 will experience the same loading waveform, but with a time shift that can be figured from Fig. A1.

Equating these angles gives the time that blade b_2 passes the reference blade on rotor 1: $t' = -2\pi b_2/B_2(\Omega_1 + \Omega_2)$. The effect on the source is to change $\exp(-i\omega_k t)$ to $\exp[-i\omega_k(t - t')]$. With $\omega_k = k B_1(\Omega_1 + \Omega_2)$, this adds $-2\pi k b_2 B_1/B_2$ to the phase in Eq. (A15).

When these two phase terms are inserted in Eq. (A15), the fields of the B_2 blades are summed, and all load harmonics are included, we find that the total signal

$$p = \sum_{k=-\infty}^{\infty} \sum_{b_2=1}^{B_2} p_k(b_2) \quad (A16)$$

includes a double sum of the form

$$\sum_{n=-\infty}^{\infty} f_n \sum_{b_2=1}^{B_2} \exp \left[-i2\pi \frac{b_2}{B_2} (n + k B_1) \right] \quad (A17)$$

The inner sum is B_2 for $(n + k B_1)$ equal to an integer multiple of B_2 and zero otherwise. Therefore, the double sum can be reduced to

$$B_2 \sum_{m=-\infty}^{\infty} f_{m B_2 - k B_1}$$

With this result, Eqs. (A4), (A15), and (A17) become Eqs. (1-5). Note also that, for the steady loading case (where only the $k=0$ term survives), these equations reduce to those derived in Ref. 3 for the observer at $\phi=0$. The sign convention for k_y has been changed for reasons described in Ref. 6.

References

- Hubbard, H. H., "Sound from Dual-Rotating and Multiple Single-Rotating Propellers," NACA TN 1654, 1948.
- Hanson, D. B., "Compressible Helicoidal Surface Theory for Propeller Aerodynamics and Noise," *AIAA Journal*, Vol. 21, June 1983, pp. 881-889.
- Hanson, D. B., "Helicoidal Surface Theory for Harmonic Noise of Propellers in the Far Field," *AIAA Journal*, Vol. 18, Oct. 1980, pp. 1213-1220.
- Hanson, D. B., "Influence of Propeller Design Parameters on Far-Field Harmonic Noise in Forward Flight," *AIAA Journal*, Vol. 18, Nov. 1982, p. 1313.
- Hanson, D. B., "Compressible Lifting Surface Theory for Propeller Performance Calculation," *Journal of Aircraft*, Vol. 22, Jan. 1985, pp. 19-27.
- Hanson, D. B., "Near-Field Frequency-Domain Theory for Propeller Noise," *AIAA Journal*, Vol. 23, April 1985, pp. 499-504.
- Morse, P. M. and Ingard, K. U., *Theoretical Acoustics*, McGraw-Hill Book Co., New York, 1968.
- Goldstein, M. E., *Aeroacoustics*, McGraw-Hill Book Co., New York, 1976.
- Tyler, J. M. and Sofrin, T. G., "Axial Flow Compressor Noise Studies," *SAE Journal*, Vol. 70, 1962, pp. 309-332.
- Block, P. J. W., "Installation Noise Measurements of Model SR and CR Propellers," NASA TM 85790, May 1984.
- Hanson, D. B., "A Unified Analysis of Fan Stator Noise," *Journal of the Acoustical Society of America*, Vol. 54, No. 6, 1973, pp. 1571-1591.
- Amiet, R. K., "Effects of Compressibility in Unsteady Airfoil Lift Theories," *Unsteady Aerodynamics*, edited by R. B. Kinney, Proceedings of a Symposium on Unsteady Aerodynamics, University of Arizona, Tucson, March 1975, pp. 631-653.
- Goldstein, S., "On the Vortex Theory of Screw Propellers," *Proceedings of the Royal Society of London*, Vol. A123, 1929.
- Weisbrich, A. L., Godston, J., Bradley, E., "Technology and Benefits of Aircraft Counter Rotation Propellers," NASA CR-168258, 1982.
- Silverstein, A., Katzoff, S., and Bullivant, W. K., "Downwash and Wake Flow Behind Plain and Flapped Airfoils," NACA Tech. Rept. 651, 1939.